Allosteric Control of Gating Mechanisms Revisited: The Large Conductance Ca^{2+}-Activated K^+ Channel

Rafael A. Rosales[†*] and Wamberto A. Varanda[‡]
[†]Department of Physics and Mathematics, Faculdade de Filosofia Ciências e Letras de Ribeirão Preto, and [‡]Department of Physiology, Faculdade de Medicina de Ribeirão Preto, University of São Paulo, Ribeirão Preto/SP Brazil

ABSTRACT Large-conductance Ca^{2+}-activated K^+ channels (BK) play a fundamental role in modulating membrane potential in many cell types. The gating of BK channels and its modulation by Ca^{2+} and voltage has been the subject of intensive research over almost three decades, yielding several of the most complicated kinetic mechanisms ever proposed. A large number of open and closed states disposed, respectively, in two planes, named tiers, characterize these mechanisms. Transitions between states in the same plane are cooperative and modulated by Ca^{2+}. Transitions across planes are highly concerted and voltage-dependent. Here we reexamine the validity of the two-tiered hypothesis by restricting attention to the modulation by Ca^{2+}. Large single channel data sets at five Ca^{2+} concentrations were simultaneously analyzed from a Bayesian perspective by using hidden Markov models and Markov-chain Monte Carlo stochastic integration techniques. Our results support a dramatic reduction in model complexity, favoring a simple mechanism derived from the Monod-Wyman-Changeux allosteric model for homotetramers, able to explain the Ca^{2+} modulation of the gating process. This model differs from the standard Monod-Wyman-Changeux scheme in that one distinguishes when two Ca^{2+} ions are bound to adjacent or diagonal subunits of the tetramer.

INTRODUCTION

The kinetic analysis of the gating of ion channels has been the subject of extensive research over several decades. The prevailing approach consists in modeling the dynamics of a single channel as a finite state Markov process. A central issue has therefore been the estimation of the infinitesimal generator, containing the rates that govern the transitions among the states of a qualitative reaction scheme. In particular, the gating of single large-conductance Ca^{2+}-activated K^+ (BK) channels and its dependency on Ca^{2+} and voltage has deserved special attention (1–9). This is partly due to the ubiquitous presence of these channels and to the high signal/noise ratio of single BK data. BK channels are homotetramers constituted by four α-subunits, each one with a Ca^{2+} bowl region involved in Ca^{2+} binding and regulatory β-subunits. Hill's coefficient for the open probability as a function of intracellular Ca^{2+} concentration is ~2–5, a fact that strongly suggests the allosteric character of Ca^{2+} as a modulator of BK channel gating. Based on the theory of allosteric cooperativism for homotetrameric proteins, Cox et al. (4) proposed a 55-state plausible gating model for BK channels. In this model, each α-subunit can assume two conformations, each of which may bind a single Ca^{2+} ion. Assuming that adjacent or diagonally Ca^{2+} bound subunits are indistinguishable from one another, the model can be reduced to 25 states. Further, if one assumes that the conformational changes that lead to channel opening occur simultaneously in all four subunits, i.e., that they are highly concerted, then the resulting model is further reduced to the 10-state mechanism

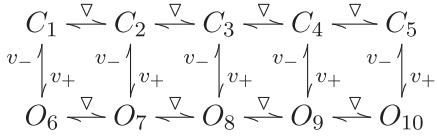

where C_i and O_i denote, respectively, closed and open states. Transitions marked by ∇ are Ca^{2+}-dependent and those marked by v_- and v_+ depend upon membrane hyperpolarization and depolarization, respectively. This scheme is equivalent to the well-known Monod-Wyman-Changeux (MWC) model for allosteric homotetramers (10), if one assumes that the binding of a Ca^{2+} ion to a given subunit does not affect the subsequent binding steps.

Despite being relatively simple, the voltage-dependent MWC model described above is able to reproduce several properties derived from macroscopic measurements such as the monoexponential activation and relaxation of macroscopic currents as well as the Boltzmann shaped conductance-voltage relations for a wide range of Ca^{2+} and voltage conditions (4,7,8,11). This model, however, fails to predict the experimental findings at high saturating Ca^{2+} concentrations. Some improvements were brought about by relaxing the independence between subsequent Ca^{2+} binding steps, leading to a general 10-state MWC model in which each binding constant may take different values from the others. This generalized model also proved to be useful in the analysis of steady-state single channel data, inspiring several of the gating mechanisms considered by the literature (12–14), the authors of which actually also considered the full 55-state model as a starting point. These models greatly expanded

Submitted September 25, 2008, and accepted for publication February 19, 2009.

*Correspondence: rrosales@ffclrp.usp.br

Editor: Richard W. Aldrich.

0006-3495/09/05/3987/10 $2.00

doi: 10.1016/j.bpj.2009.02.042

the predictive power of previously proposed mechanisms (see (3)), such as the presence of multiple gateways between open and closed classes of states (modal gating), fast flickers, and high positive open-closed correlations at saturating Ca^{2+} concentrations. To achieve this, however, some of the most complicated gating schemes ever proposed were used. In these models, a large number of states are arranged in two planes according to whether these correspond to open or closed conformations of the tetramer. Consistently with the MWC model, Ca^{2+} modulated transitions between states of the same plane are cooperative, whereas those across planes leading to closing and opening are concerted and voltage-dependent. These models present a large number of parameters, being in some cases up to 46 (scheme X in (13) shown here in Fig. 1 as scheme II) or 66 (scheme II in (14), shown here in Fig. 1 as scheme IV).

In this article, we reexamine the validity of the two-tiered models, by analyzing large data sets (40×10^6 samples) at five different Ca^{2+} concentrations. Several models, including those in the literature (4,12,14), are compared by means of the Bayesian information criterion (BIC). Our analysis is made by representing the observations as the realization of an aggregated hidden Markov model and extending previous Markov-chain Monte Carlo (MCMC) methods (15), which allow the simultaneous analysis of data at several Ca^{2+} concentrations. These techniques enable us to use all the information available in the data by considering every single observation in the inferential process. As a result, the model with highest BIC rank resulted in a simple two-tiered model, referred to as scheme III in Cox et al. (4).

THEORY AND METHODS

Modeling approach

The gating process is modeled by representing the channel as a homogeneous Markov process, $\{Z(t): t \geq 0\}$, with values on the set $\mathfrak{S}$ of kinetically distinguishable states of a gating mechanism. $\mathfrak{S}$ may be partitioned into sets of states sharing the same conductance, usually $\mathfrak{O} = \{O_i\}$, $i = 1, \ldots, n_o$, the set of open states, and $\mathfrak{L} = \{C_i\}$, $i = 1, \ldots, n_c$, the set of closed states. Let $n = n_o + n_c$. The continuous time process $Z(t)$ is sampled at N evenly spaced time periods, of duration δ, producing the δk-skeleton, $Z_{\delta k}$, $k = 1, \ldots, N$. For simplicity, hereafter we denote $Z_{\delta k}$ simply by Z_k. The gating process is then characterized by a transition probability matrix P with entries $p_{ij} = \mathbb{P}(Z_k = j \mid Z_{k-1} = i)$, and an initial distribution $\mathbb{P}(Z_0 = i) = p_i$, $i, j, \in \mathfrak{S}$. The process Z_k is, however, not directly observed in a patch-clamp experiment. As a first approximation, each observation y_k, $1 \leq k \leq N$, may be thought of as

$$y_k = f(Z_k) + g(Z_k)\xi_k, \tag{1}$$

where $f(Z_k) = \mu_{\mathfrak{O}}$ if $Z_k \in \mathfrak{O}$ and $f(Z_k) = \mu_{\mathfrak{L}}$ otherwise, and also $g(Z_k) = \mu_{\mathfrak{O}}$ or $g(Z_k) = \mu_{\mathfrak{L}}$. Here $\mu_{\mathfrak{O}}$ and $\mu_{\mathfrak{L}}$ denote the mean current values (in pA) when the channel is open and closed, respectively, and $\mu_{\mathfrak{O}}$, $\mu_{\mathfrak{L}}$ the standard deviations of the current fluctuations associated to each conformation. The values ξ_k, $1 \leq k \leq N$, are independent and identically distributed standard normal random variables.

The above model, referred to as aggregated hidden Markov model in Rosales (15), is actually a generalization of the hidden Markov model initially described by Chung et al. (16). Several other extensions including dependent background noise and filtering, most notably by Ventakaramanan and Sigworth (17) and de Gunst et al. (18), have since then appeared. Dependencies originate from the properties of the processes that give rise to the background noise, and due to low band-pass filtering, used to restrict the signal power at high frequencies and prevent aliasing. The filtering characteristics of the recording apparatus may be modeled via a finite impulse response filter with coefficients a_k, $k = 0, \ldots, l-1$, obtained by measuring the step response of the patch-clamp system. Denote by * the convolution operation, then the anti-aliasing step can be accounted for as $(a * f(Z))_k = \sum_{i=0}^{l-1} a_k f(Z_{k-i})$. Let c_k, $1 \leq k \leq N$ denote the correlated background noise sequence. The correlations present in c_k may also be modeled by using a finite impulse response filter of order u, determined by the coefficients b_k, $k = 0, \ldots, u-1$. This filter is estimated from the autocorrelations present in c_k, i.e., from a data segment without channel openings, via a Yule-Walker system, efficiently solved by means of the Levinson-Durbin algorithm ((19), algorithm 4.7.2). The background correlations may then be removed by convolution with the inverse of b_k, denoted here as ζ_k (that is, $\xi_k = (\zeta * c)_k$).

This preprocessing step produces the sequence $x = (x_k)$, $1 \leq k \leq N$, of whitened observations. Following Eq. 1, x_k is given by

$$x_k = (\zeta * y)_k = (\zeta * a * f(Z))_k + \sigma\xi_k, \tag{2}$$

where it has been assumed that the variance of the background noise is state-independent, i.e., that $g(Z_k) = \sigma$. A general approach to class-dependent variances may also be incorporated into the Bayesian treatment at the cost of extra computational burden (see (18)).

In practice, we found that $u = 3$ was sufficient to model the correlations present in the background noise. Also, $l = 5$ gave an appropriate description for the filtering effects. In this case, $\zeta * a$ in Eq. 2 resulted in a filter with an effective lag of $u + l = 8$ coefficients.

Statistical treatment

Denote by $\theta = (\mu_{\mathfrak{O}}, \mu_{\mathfrak{L}}, \sigma, P, p) \in \Omega$, the parameters of an aggregated hidden Markov model associated to a particular gating mechanism, and $\Omega = \mathbb{R}^{n_o} \times \mathbb{R}^{n_c} \times (0, \infty)^n \times [0,1]^{n \times n} \times [0,1]^n$, the space spanned by θ. The estimation of θ is made from a Bayesian perspective by using MCMC methods. Briefly, given a sequence of gating states $z = (z_k)$, $z_k \in \mathfrak{S}$, and observations $x = (x_k)$, $1 \leq k \leq N$, the above formulation describes the likelihood for the data,

$$\mathcal{L}(x, z|\theta) = \mathbb{P}(X = x|\theta, Z = z)\mathbb{P}(Z = z|\theta). \tag{3}$$

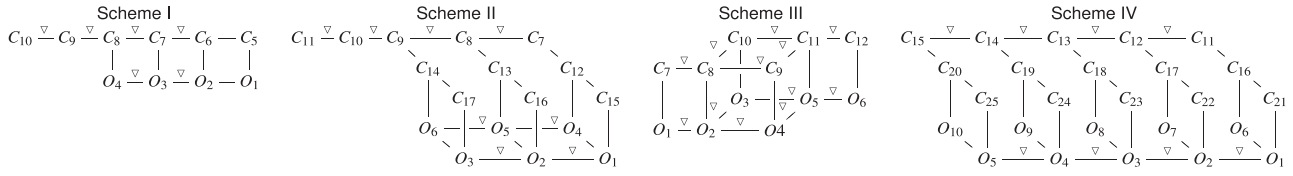

FIGURE 1 Allosteric gating mechanisms. Scheme I corresponds to scheme VII in Rothberg and Magleby (12), scheme II to scheme X in Rothberg and Magleby (13), and scheme IV to scheme II in Rothberg and Magleby (14). Scheme III corresponds to a simpler two-tiered gating mechanism described as scheme III in Cox et al. (4). All transitions marked with ∇ are Ca^{2+}-dependent.

Following Eq. 2, the first term at the right of Eq. 3 is just a product of N normal distributions with mean $\zeta^* a^* f(z)$, and standard deviation σ. The Markov property on Z determines the distribution $\mathbb{P}(Z = z \mid \theta)$ uniquely in terms of P and p. The joint posterior distribution for θ and z is proportional to the product of the likelihood in Eq. 3 and the prior distribution, that is

$$\mathcal{P}(\theta, z|x) \propto \mathcal{L}(x, z|\theta)\mathbb{P}(\Theta = \theta).$$

Given a gating mechanism, this formulation provides a consistent description of the fit of any model configuration for the mechanism, i.e., any pair of values (θ, z). Most characterizations of the distribution of (θ, z) are formulated as the expectation of a function h with respect to $\mathcal{P}$,

$$\mathbb{E}[h(\Theta, Z) \mid x] = \int_{\Omega}\int_{\mathfrak{S}^N} h(\theta, z)\mathcal{P}(d\theta, dz \mid x).$$

The main interest here is directed toward the estimation of P, namely by taking $h(\Theta, Z) = (\Theta, Z)$. In this case, a estimate for the transition probabilities of the hidden process, P, is simply given by its posterior expected value. The necessary integrations are numerically performed via MCMC, more precisely by using the Gibbs sampler described in Rosales (15). The sampler consists essentially of an ergodic Markov chain $\{\Theta^r, Z^r\}$, $r \in \mathbb{N}$, with $\mathcal{P}$ as its invariant distribution. In this case, because of the ergodic theorem, for any initial values (θ^0, z^0), $R^{-1}\sum_{r=1}^{K}(\theta^r, z^r) \to \mathbb{E}[(\Theta, Z) \mid x]$, as $R \to \infty$. Thus, our MCMC estimate for P is simply given by

$$\widehat{P}_R = \sum_{r=b+1}^{R} \frac{P^r}{R - (b + 1)},$$

where P^r denotes the r^{th} MCMC sample for P, and to allow for the convergence of the sampler, we discarded the first b MCMC iterations. This initial period was assessed by using the Raftery-Lewis and the Heidelberger-Welch convergence diagnostics, implemented in the BOA software (http://www.public-health.uiowa.edu/boa).

The estimate for P, obtained at the limited resolution imposed by δ, say P_δ, may be used to compute the transition rate matrix

$$Q_\delta = (I - P_\delta)/\delta, \tag{4}$$

with elements q_{ij}, $i, j \in \mathfrak{S}$. Let $\widehat{p}_{ij}$ denote the elements of $\widehat{P}_R$, then, the estimates for the transition rates are given by

$$\widehat{q}_{ij} = \widehat{p}_{ij}/\delta, \quad \widehat{q}_{ii} = \left(1 - \widehat{p}_{ii}\right)/\delta.$$

It is important to stress that Q_δ has to be taken only as an approximation to the infinitesimal generator of the continuous process $Z(t)$, i.e., $\lim_{\delta \to 0^+} Q_\delta$. Q_δ, however, contains all the relevant information to characterize the dynamical properties of an ion channel at this temporal resolution. To simplify notation, Q_δ and P_δ will be denoted throughout as Q and P. Standard Q-matrix methods (see (20,21)) were used here to compute: 1), the dwell-time distributions in $\mathfrak{O}$, $\mathfrak{U}$; and 2), the bivariate distribution of the open-closed dwell-times. Computations were carried out by using Maple 7 (Maplesoft, Waterloo Maple, Waterloo, Ontario).

All the MCMC runs made only considered as free parameters the transition rate matrix P and the initial distribution p of the hidden process. The values $\mu_{\mathfrak{U}}$, $\mu_{\mathfrak{O}}$, and σ were kept constant and equal to values obtained from a standard all-points amplitude histogram (see (22)).

Global analysis

The way in which Ca^{2+} modulates the gating of BK channels may be studied by analyzing separately single channel data at several intracellular Ca^{2+} concentrations. This, however, has the disadvantage that at a particular condition, the channel only visits a given set of the gating states rendering almost no information about some other possible transitions. This may happen, for instance, at low or high saturating Ca^{2+} concentrations. It is therefore desirable to be able to gather most of the information available by performing a global analysis, producing a single estimate for P_δ. This is accomplished as follows. The Gibbs sampler used here produces a sequence of transition probability matrices, $\{P^k\}$, by drawing each row, P_i, $1 \le i \le n = n_o + n_c$, from the full conditional density

$$\pi(P_i \mid \theta(-P_i), x, z)dP_i = C\mathcal{L}(x, z \mid \theta)\mathbb{P}(\Theta = \theta)$$
$$C = \int_{\mathcal{D}_i} \mathcal{L}(x, z \mid \theta)\mathbb{P}(\Theta = \theta)dP_i$$

for $\mathcal{D}_i = \{0 < p_{ij} < 1 : \sum_j p_{ij} < 1\}$. Here $\theta(-P_i)$ is used to denote all the parameters in θ but P_i. By considering a Dirichlet distribution as a priori with parameter $e_i = (e_{i1}, \ldots, e_{in})$, $e_{ij} > 0$, one can, in fact, compute the integral above, yielding

$$\pi(P_i \mid \theta(-P_i), x, z) = \frac{\Gamma\left(\sum_j c_{ij} + e_{ij}\right)}{\prod_j \Gamma\left(c_{ij} + e_{ij}\right)} \prod_j p_{ij}^{c_{ij} + e_{ij} - 1},$$

a Dirichlet distribution with parameter $c_i + e_i = (c_{i1} + e_{i1}, \ldots, c_{in} + e_{in})$. The terms $c_{ij} \ge 0$,

$$c_{ij} = \sum_{k=1}^{N-1} \mathbf{1}_{\{Z_k = i\}}\mathbf{1}_{\{Z_{k+1} = j\}},$$

arise from the likelihood function of a given gating sequence z, and stand for the number of transitions from state i to state j, $i; j \in \mathfrak{S}$. Suppose M data sets, each at a different Ca^{2+} concentration, are being analyzed. Denote by c_{ij}^m, $1 \le m \le M$, the number of transitions $i \to j$ present at the m^{th} segment. The total number of transitions of type $i \to j$ may be computed as

$$c_{ij} = \sum_{m=1}^{M} c_{ij}^m / R_m, \tag{5}$$

with $R_m = [Ca^{2+}]_m/[Ca^{2+}]_R$, and $[Ca^{2+}]_m$ as the Ca^{2+} concentration at the m^{th} file and $[Ca^{2+}]_R$ the concentration at an arbitrary reference condition. This allows us to express a single estimate for the transition rate matrix with respect to this condition.

Suppose any given transition $i \to j$ is Ca^{2+}-dependent. The procedure above is justified because from Eq. 4 one has that $p_{ij} = q_{ij}[Ca^{2+}]/\delta$. It should be noted that the changes introduced by Eq. 5 do not compromise the ergodicity of the Gibbs sampler.

Model choice

Denote by $x^i = (x_1^i, \ldots, x_{N_i}^i)$, $1 \le i \le M$, several independent data sets. Models considered here were ranked by using the global (i.e., by analyzing all M data sets) BIC score

$$\text{BIC} = -2\sum_{i=1}^{M} \ln\left(\mathcal{L}\left(x^i \mid \theta^*\right)\right) + 2N_\theta \sum_{i=1}^{M} \ln(N_i).$$

Here N_θ stands for the number of parameters associated to a model, N_i denotes the number of observations of the i^{th} data set, $\mathcal{L}(x \mid \theta^*)$ is the marginal likelihood

$$\mathcal{L}(x \mid \theta^*) = \int_{\mathfrak{S}^N} \mathcal{L}(x, dz \mid \theta^*),$$

and θ^* is the MCMC estimate for θ. Marginalization may be performed efficiently by means of the standard Baum-Welch recursion. If $\mu_{\mathfrak{U}}$, $\mu_{\mathfrak{O}}$, and σ are fixed, then N_θ equals the number of transition rates that have to be estimated.

Dwell-time densities

Dwell-time densities are computed by using the MCMC estimate for the Q-matrix and standard Q-matrix methods (20,21). This includes the

single-class dwell-time distributions seen later in Fig. 4 and the joint open-closed dwell-time densities seen later in Fig. 5. Let $f_{\mathfrak{Q},\mathfrak{O}}$ denote the joint density for open-closed dwell-time pairs, and $f_{\mathfrak{Q}}$ and $f_{\mathfrak{O}}$ the marginal densities for the closed class and the open class, respectively. Following Magleby and Song (23), the dependency-difference plots seen later in Fig. 6 are computed as

$$d(x,y) = f_{\mathfrak{Q},\mathfrak{O}}(x,y)^{1/2} - f_{\mathfrak{Q}}(x)^{1/2} f_{\mathfrak{O}}(y)^{1/2}, \quad (6)$$

and the difference plots seen later in Fig. 7 as

$$\left\{ f_{\mathfrak{Q},\mathfrak{O}}(x,y) / [f_{\mathfrak{Q}}(x) f_{\mathfrak{O}}(y)] \right\}^{1/2} - 1. \quad (7)$$

So, if $d(x, y) > 0$, then the given x, y dwell-time pair is positively correlated.

Dwell-time densities from standard filter and threshold analysis such as those seen later in Fig. 8 are computed by using the idealized dwell-time data in conjunction with kernel-density estimation methods (24).

Single channel recordings

Currents through single BK channels were measured by using the patch-clamp technique in the inside-out configuration, as described in Carnio and Varanda (25). Freshly isolated Leydig cells from mice were plated onto small coverslips and transferred to a recording chamber continuously perfused with Hanks' solution (145 mM NaCl; 4.6 mM KCl; 1.2 mM $MgCl_2$; 1.6 mM $CaCl_2$; 10 mM; 10 mM glucose; 5 mM $NaHCO_3$; pH 7.4). Recording pipettes were filled with (mM): 150 KCl; 1 $MgCl_2$; 5 HEDTA; 10 HEPES (pH 7.3 adjusted with KOH); 10^{-7} M $CaCl_2$ and had resistance ≥ 12 MΩ. At first, channels were observed with the cell-attached configuration, and then the pipette was retracted to achieve the inside-out configuration. A holding potential of +60 mV was applied and single channel events recorded. Under these conditions, the steady-state open probability is well above 0.95, so that recordings with more than one channel could be easily discarded. If only one channel was present, then the bath solution was changed to the same solution inside the pipette, but having free calcium concentration of 10^{-7} M, 5×10^{-7} M, 10^{-6} M, 3×10^{-6} M, and 10^{-5} M as desired. Free calcium concentrations were calculated by using the program Webmax Extended (www.stanford.edu/~cpatton/webmax/webmaxcE.htm). Single channel activity was now recorded at +30 mV. This potential was chosen because most of the single channel modeling concerning the Ca^{2+} modulation of BK channel kinetics was done at +30 mV, and this also gives a suitable signal/noise ratio for the analysis with hidden Markov models. Current was measured with Axopatch 200B (Axon Instruments, Foster City, CA), filtered at 10 KHz (−3 dB, eight-pole Bessel filter), sampled at 100 KHz via a Digidata 1200 interface (Axon Instruments) and stored on hard disk for off-line analysis. Five data sets, each at one Ca^{2+} concentration mentioned above, were simultaneously used for the global analysis described in the modeling section. Each data set contained 40×10^6 samples.

As an example, Fig. 2 presents few brief segments of the raw data used in the global analysis. This figure also displays the corresponding sequence of hidden states predicted in one of the iterations of the MCMC sampler. Close inspection of these realizations may be used to identify the transitions involved in particular features such as fast flickers.

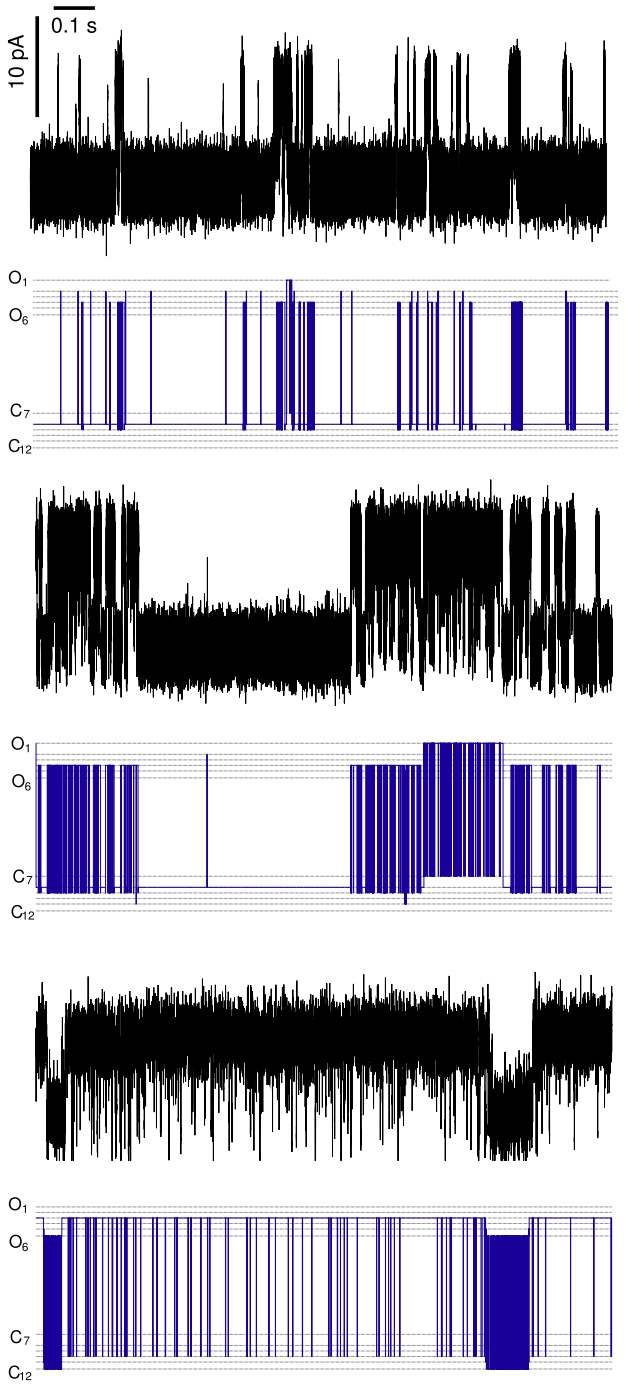

FIGURE 2 Noisy traces from top to bottom present brief data segments at 1×10^{-7}, 3×10^{-6}, and 1×10^{-5} M Ca^{2+}, respectively. Channel openings correspond to upward deflections. Straight-line traces display a possible realization of the underlying gating process. The hidden realization drawn by the MCMC sampler corresponds to just one of 15,000 realizations produced while iterating the MCMC algorithm by using the KNF model. Different conductances were artificially assigned to each state as an aid to enhance visualization (data was, however, analyzed by assuming just two conductances in accordance to the KNF model).

RESULTS

Model ranking

Five data sets containing the activity of a single BK channel at different Ca^{2+} concentrations were simultaneously analyzed. The analysis was made by considering several gating mechanisms already reported in the literature, shown

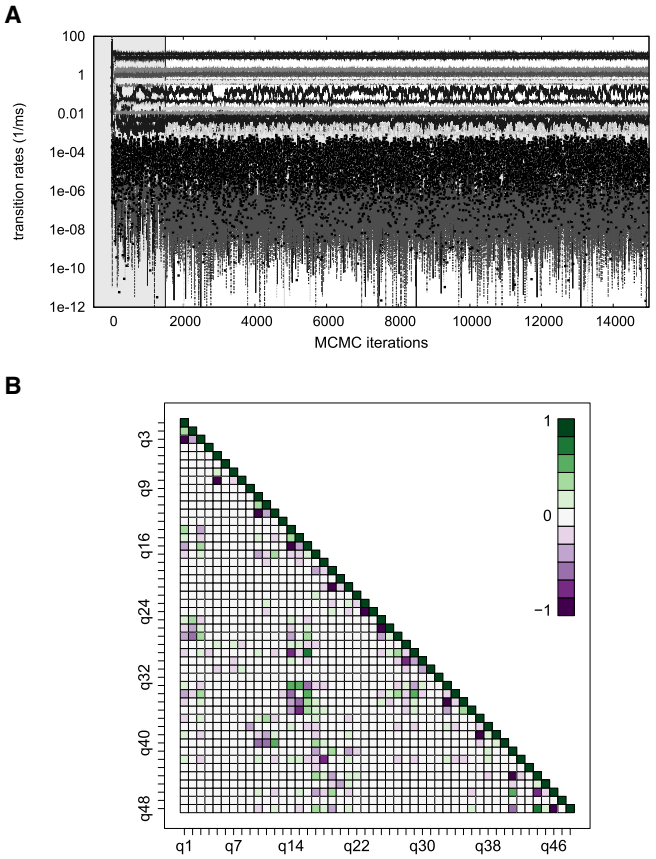

FIGURE 3 (*A*) MCMC samples for the Q_δ matrix obtained by the global analysis of single channel data at five different Ca^{2+} concentrations for the KNF gating scheme. The shaded area shows the iterations discarded to allow for the relaxation period of the MCMC sampler. The nondiagonal entries of the Q_δ matrix are not displayed. (*B*) Cross-correlation matrix for the MCMC samples obtained by the global analysis performed with the KNF scheme. Labels denoted by $q1$, $q2$, …, $q48$ correspond to the following ordering of the allowed transitions between the states in scheme III: $q1 = O_1 \rightarrow O_1$, $q2 = O_1 \rightarrow O_2$, $q3 = O_1 \rightarrow C_7$, $q4 = O_2 \rightarrow O_2$, … (i.e., O precedes C). Note that panel *B* includes the cross-correlations for all the entries in the Q_δ matrix, including the diagonal.

in Fig. 1. The first model, referred here to as scheme I, corresponds to scheme VII in Rothberg and Magleby (12). This scheme was chosen because it represents one of the simplest mechanisms that was initially able to reproduce a fair amount of the properties found while analyzing single channel data (1–3). Interestingly, the reaction scheme of this model is also consistent with the standard MWC model. Despite of its qualities, scheme I failed to reproduce the kinetics at high Ca^{2+} such as the presence of fast flickers. To overcome these problems Rothberg and Magleby (13) proposed the two-tiered model, represented by scheme II in Fig. 1. This model may be seen as a simplified version of the initial 55-state mechanism for a homotetramer with a Ca^{2+} binding site per subunit, in which every closed conformation could lead to opening. This model was able to predict an excess of brief open intervals adjacent to longer closed intervals observed at high Ca^{2+} conditions. Scheme III presents a model introduced by Cox et al. (4). This model is a direct extension of the 10-state MWC model for which the conformations that correspond to a channel with two bound Ca^{2+} in adjacent or diagonal subunits can now be distinguished (states C_9, C_{10} and O_3, O_4, see scheme III in Fig. 1). The same as in Cox et al. (4), we will refer to scheme III as the KNF model, which actually stands as an abbreviation for Khosland-Nemethy-Filmer. This terminology was presumably used because this model has extra Ca^{2+}-dependent concerted transitions, not present in the MWC model. Scheme IV in Fig. 1 was proposed in Rothberg and Magleby (14) as an extension to scheme II, to account for both Ca^{2+} and voltage regulation of BK gating.

The transition rates for schemes I–IV were estimated as described in Theory and Methods via MCMC. The traces in Fig. 3 *A* show the actual samples for the 36 transition rates of scheme III (diagonal entries are not shown). The MCMC sampler seems to converge after approximately the first 1500 iterations, a value that was quantitatively assessed by means of several convergence tests mentioned in Theory and Methods. Fig. 3 *B* displays the cross-correlation matrix for the transition rates computed directly by using the MCMC samples after convergence. This matrix shows that there are quite a few significant positive and negative correlations. For example, the entry (q_{16}, q_{29}) has a correlation of 0.8, and the entry (q_{18}, q_{42}) has a correlation of -0.8. This suggests that the KNF model does provide a sensible parameterization for the underlying dynamics.

The rate estimates for schemes I–IV were used to rank these models according to their BIC values. Models with smaller values are preferred, being the smallest value equal to 354118975.798 the one corresponding to scheme III. To facilitate the comparison, denote by ΔBIC_i the difference of the BIC value for the i^{th} model minus the BIC for scheme III. So as a result from our analysis we found that $\Delta BIC_{IV} = 2038.779$, $\Delta BIC_{II} = 28454.068$, and $\Delta BIC_I = 173797.626$. These values yield thus the rank order

$$\text{III} > \text{IV} > \text{II} > \text{I}.$$

Interestingly, this order is consistent with the results in the literature (12–14), namely: IV > II > I. All results reported hereafter will refer to those obtained by the estimates for the best model, that is, scheme III. The actual estimate for the transition rate matrix is shown in Table 1. These values were computed by taking the average of the last 13,500 samples out of a total of 15,000 MCMC iterations (displayed in Fig. 1). Ca^{2+}-dependent transition rates are given in $ms^{-1} \times 10^{-7}\ M^{-1}$, whereas Ca^{2+}-independent rates are in ms^{-1}.

This matrix constitutes the basis for all further analyses and model predictions presented next.

KNF model predictions

Predictions made with scheme III can be described in several ways. To facilitate the presentation, results shown hereafter

TABLE 1 Estimated *Q*-matrix for scheme III

Transition	Rate constant	Transition	Rate constant
$O_1 \overset{\nabla}{\rightarrow} O_2$	$0.423e^{-4}$	$O_1 \rightarrow C_7$	0.541
$O_2 \rightarrow O_1$	$0.128e^{-2}$	$O_2 \overset{\nabla}{\rightarrow} O_3$	$0.73e^{-4}$
$O_2 \overset{\nabla}{\rightarrow} O_4$	$0.581e^{-3}$	$O_2 \rightarrow C_8$	1.956
$O_3 \rightarrow O_2$	$0.229e^{-4}$	$O_3 \overset{\nabla}{\rightarrow} O_5$	$0.32e^{-4}$
$O_3 \rightarrow C_{10}$	0.352	$O_4 \rightarrow O_2$	$0.163e^{-3}$
$O_4 \overset{\nabla}{\rightarrow} O_5$	$0.821e^{-4}$	$O_4 \rightarrow C_9$	0.912
$O_5 \rightarrow O_3$	1.229	$O_5 \rightarrow O_4$	0.134
$O_5 \overset{\nabla}{\rightarrow} O_6$	$0.512e^{-2}$	$O_5 \rightarrow C_{11}$	13.41
$O_6 \rightarrow O_5$	0.442	$O_6 \rightarrow C_{12}$	12.352
$C_7 \rightarrow O_1$	9.13	$C_7 \overset{\nabla}{\rightarrow} C_8$	$0.823e^{-2}$
$C_8 \rightarrow O_2$	$0.11e^{-1}$	$C_8 \rightarrow C_7$	$0.1e^{-2}$
$C_8 \overset{\nabla}{\rightarrow} C_9$	$0.418e^{-2}$	$C_8 \overset{\nabla}{\rightarrow} C_{10}$	$0.422e^{-6}$
$C_9 \rightarrow O_4$	8.051	$C_9 \rightarrow C_8$	1.194
$C_9 \overset{\nabla}{\rightarrow} C_{11}$	$0.46e^{-2}$	$C_{10} \rightarrow O_3$	8.137
$C_{10} \rightarrow C_8$	$0.193e^{-1}$	$C_{10} \overset{\nabla}{\rightarrow} C_{11}$	$0.337e^{-3}$
$C_{11} \rightarrow O_5$	1.08	$C_{11} \rightarrow C_9$	$0.453e^{-1}$
$C_{11} \rightarrow C_{10}$	$0.39e^{-3}$	$C_{11} \overset{\nabla}{\rightarrow} C_{12}$	$0.99e^{-4}$
$C_{12} \rightarrow O_6$	8.262	$C_{12} \rightarrow C_{11}$	$0.108e^{-2}$

Transitions marked with ∇ are calcium-dependent. Ca^{2+}-dependent rates are given in $ms^{-1} \times 10^{-7}\ M^{-1}$. Ca^{2+}-independent rates are in ms^{-1}. Diagonal entries are not shown. Rates corresponding to nonallowed transitions are equal to 0.

will be restricted to tree representative Ca^{2+} concentrations: low corresponding to 1×10^{-7} M, intermediate corresponding to 3×10^{-6} M, and high to 1×10^{-5} M.

An essential characterization of the dynamics of single channels is given by the distributions of the time spent at a given set of states, for instance in the closed and the open classes. Fig. 4 shows the dwell-time densities in the open class $\mathfrak{O} = \{O_1, \ldots, O_6\}$ and the closed class $\mathfrak{C} = \{C_7, \ldots, C_{12}\}$ for the KNF model. At low Ca^{2+}, the closed class density is essentially dominated by the sojourns in state C_8, followed then by those in state C_7. The excess of dwell times in these two states is determined by the two maxima of the density in Fig. 4. The density for the open class at this condition is dominated by sojourns in state O_1. At the intermediate Ca^{2+} condition, the closed density lost its slowest component. The component with highest area corresponds now to dwell times in C_{10}. The open class density is now characterized by the appearance of two fast components, O_5 and O_6. This density is, however, still characterized by a predominant component corresponding to sojourns in O_3. At the highest Ca^{2+} concentration, the slowest components of the closed density have been further shifted toward the left; meaning that most of the long-lasting sojourns at low Ca^{2+} concentrations have now disappeared. The most important components for the open class are O_3 and O_4, but now two very fast components O_5 and O_6 have also a substantial proportion of the dwell times. All these results are also reinforced by the values for the stationary distribution and the single-state mean lifetimes presented in Tables 2 and 3. These quantities are computed directly from the MCMC Q-matrix estimate. When considered together, they allow us to draw a detailed picture for the changes induced by Ca^{2+}. At low Ca^{2+}, the channel prefers to dwell in states C_7, C_8, and O_1. The state

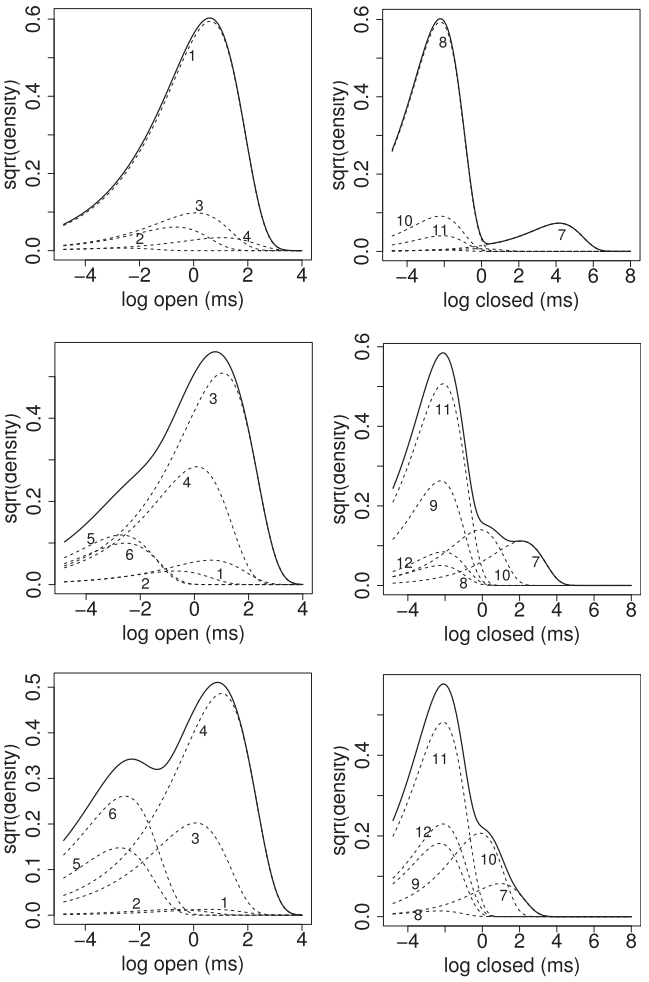

FIGURE 4 Predicted single-class log dwell-time densities at several Ca^{2+} concentrations for scheme KNF. Single state components are shown as dashed lines. Graphs at the left column display the densities for the open class, $\mathfrak{O}$, and those at the right column the densities for the closed class, $\mathfrak{C}$. Rows from top to bottom present the densities at 1×10^{-7} M, 3×10^{-6} M, and 1×10^{-5} M Ca^{2+}, respectively. Numbers associated to each component indicate the actual state within the class, for instance "1" corresponds to O_1, "7" to C_7, and so on (see scheme III). Plots actually show the square-root of the density.

C_7 has quite a long expected mean lifetime, and is responsible for the long closed data stretches. Long closures are briefly interrupted by transitions to O_1 via C_8 and O_2. As Ca^{2+} rises, the channel now spends most of the time at states C_{10}, and O_3, and, less frequently, at C_{10} and O_4. At the highest Ca^{2+} concentration, the channel still prefers O_3 and O_4, but the closed dwell times are almost all from sojourns in C_{11}. The intermediate open dwell times in O_3 are interrupted by very fast closures and openings associated to the transitions $C_{12} \leftrightarrow O_6$ and $C_{11} \leftrightarrow O_5$. The actual identity of the transitions is readily available from the MCMC sampler, as shown by the hidden realization in Fig. 2.

The information provided by the dwell-time distributions and the stationary distribution is complemented by the correlations between subsequent open-closed dwell-time pairs.

TABLE 2 KNF stationary probability distribution (η) and single-state mean lifetime (τ, ms) at several Ca^{2+} concentrations for the closed class

$[Ca^{2+}]$ (M)		C_7	C_8	C_9	C_{10}	C_{11}	C_{12}
1×10^{-7}	η_{C_i}	$0.368e^{-1}$	0.325	$0.113e^{-2}$	$0.132e^{-3}$	$0.42e^{-4}$	$0.22e^{-6}$
	τ_{C_i}	63.954	0.109	0.888	0.108	0.123	0.121
3×10^{-6}	η_{C_i}	$0.381e^{-3}$	0.1	$0.101e^{-1}$	$0.319e^{-1}$	$0.175e^{-1}$	$0.879e^{-3}$
	τ_{C_i}	8.253	0.107	0.106	0.886	0.122	0.121
1×10^{-5}	η_{C_i}	$0.22e^{-4}$	0.019	$0.621e^{-2}$	0.035	0.047	0.008
	τ_{C_i}	2.657	0.1	0.102	0.882	0.122	0.121

These correlations constitute useful means in the determination of the connectivity between the states of a gating mechanism from the data. The estimation of these correlations were fundamental for the approaches that lead to schemes I, II, and IV (see (12–14)). In fact, it was the failure of scheme I to predict a large correlation between open dwell times followed by fast closures (flickers), that lead Rothberg and Magleby (13,14) to consider both mechanisms II and IV. Correlations between adjacent open-closed dwell-time pairs may be computed from the joint open-closed densities such as those displayed in Fig. 5. Here, these densities correspond to the one predicted directly by the Q-matrix estimate for the KNF model. Consistently with the results for the single class distributions, as Ca^{2+} rises, the densities concentrate toward faster dwell-time components. Correlations obtained from these densities may be displayed by plotting the dependency-difference defined by Eq. 6. The actual significance of these correlations can be measured by the difference given by Eq. 7. These two quantities at the low, intermediate, and high Ca^{2+} conditions are shown, respectively, in Figs. 6 and 7. The open-closed correlations are not very much affected by Ca^{2+} changes. Interestingly, however, as Ca^{2+} increases, the most significant correlation component seems to shift gradually from fast-open fast-closed transitions to slower-open fast-closed ones. It is important to remark that these correlations are also detected by analyzing the same data with scheme IV (Fig. S1), the best model so far proposed by Rothberg and Magleby (12–14); however, this does not happen with scheme I (data not shown). A standard filter and threshold analysis at 10 KHz reveals (Fig. S2) these correlations to be a genuine feature of our data.

Model comparison

A simple way for assessing the predictive power of both scheme III and IV consists in a direct comparison of the associated single class dwell-time distributions. For brevity, results in this section are restricted to the lowest and the highest Ca^{2+} condition. Fig. 8 presents the dwell-time densities for the open and the closed classes shown in Fig. 4 for scheme III, superimposed on the densities for scheme IV and also those produced by a standard filter and threshold analysis at 7.5 KHz.

At 7.5 KHz, the threshold analysis produces an apparent excess of brief open sojourns, presumably due to background-noise threshold crossings. At the highest Ca^{2+} condition (Fig. 8, *C* and *D*), both scheme III and the threshold analysis produced quite similar dwell-time distributions. At this concentration, scheme IV detects fewer fast open transitions and predicts an excess of long-lived shut periods. At the lowest Ca^{2+} concentration, scheme IV is closer than scheme III to the threshold analysis. All three predict the existence of long-lived shut periods; however, scheme III assigns the smallest weight to these events. Although this is a substantial difference, scheme III is able to better describe the data as a whole because: 1), the log-likelihood values for the three higher Ca^{2+} conditions are much smaller than for the other models; and 2), the second-best-ranked model (scheme IV), with a similar total likelihood value to scheme III, has a much larger penalization factor because of the number of parameters associated with it.

DISCUSSION

The evidence present in our data strongly supports a large simplification of models previously used while analyzing single channel data, to describe the allosteric modulation of BK channel gating by Ca^{2+}. Indeed, the number of transitions rates in the model defined by scheme III, the model with highest BIC rank, is approximately half the number

TABLE 3 KNF stationary probability distribution (η) and single-state mean lifetime (τ, ms) at several Ca^{2+} concentrations for the open class

$[Ca^{2+}]$ (M)		O_1	O_2	O_3	O_4	O_5	O_6
1×10^{-7}	η_{O_i}	0.621	$0.184e^{-2}$	$0.446e^{-2}$	$0.997e^{-2}$	$0.305e^{-5}$	$0.81e^{-6}$
	τ_{O_i}	1.847	0.511	1.096	2.842	$0.677e^{-1}$	$0.782e^{-1}$
3×10^{-6}	η_{O_i}	$0.641e^{-2}$	$0.581e^{-3}$	0.741	$0.887e^{-1}$	$0.135e^{-2}$	$0.584e^{-3}$
	τ_{O_i}	1.843	0.506	2.835	1.093	$0.669e^{-1}$	$0.784e^{-1}$
1×10^{-5}	η_{O_i}	$0.369e^{-3}$	$0.12e^{-3}$	0.82	0.055	$0.365e^{-2}$	$0.526e^{-2}$
	τ_{O_i}	1.833	0.494	1.086	2.819	$0.651e^{-1}$	$0.787e^{-1}$

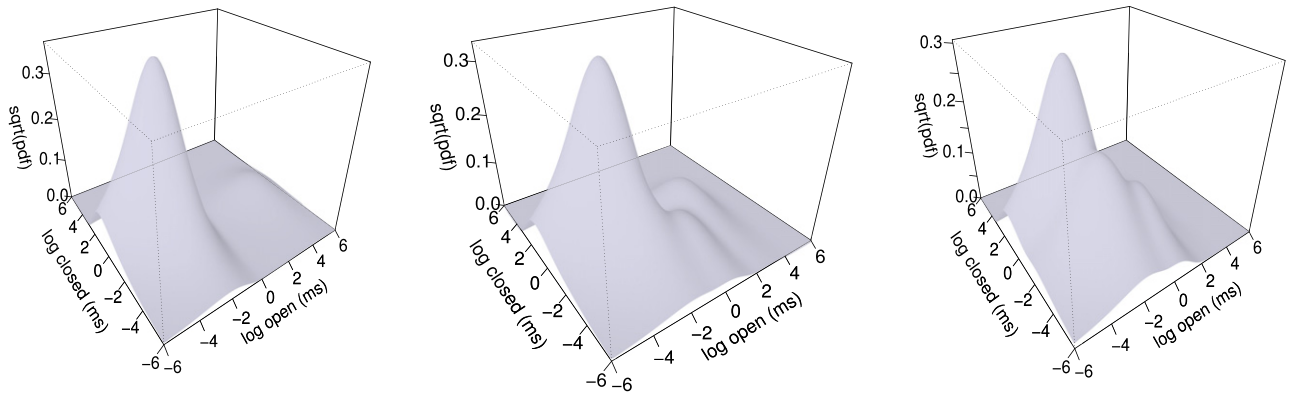

FIGURE 5 Joint log dwell-time densities at several Ca^{2+} concentration predicted by the KNF mechanism. From left to right, the Ca^{2+} concentrations are: 1×10^{-7} M, 3×10^{-6} M, and 1×10^{-5} M. Plots are shown by taking the square-root of the actual densities. Densities are computed from the global Q_δ estimate by using standard Q-matrix methods (see (21)).

of those present in schemes II and IV. The later have proven to be the most successful models in the quantitative analysis pursued by Rothberg and Magleby (13,14), being able to describe the kinetic properties of single BK channels over a wide range of Ca^{2+} conditions. Most critically, these models are able to account for flickers and highly correlated open-closed sojourn pairs, present at high saturating Ca^{2+} conditions. The results presented here show that scheme III is also able to describe these features. The material included as Supporting Material shows that the findings of both scheme III and scheme IV are in fact quite similar.

Although interesting from a statistical perspective, the results presented here may be important because they provide a simplifying view of the underling physical mechanism of BK channel gating. Both mechanisms II and IV are built on the two-tier hypothesis, an idea inspired by the initial considerations about Ca^{2+}-modulated homotetramers made by Cox et al. (4), further developed by Rothberg and Magleby (14). In this theory, a large number of closed and open states may be disposed into two separate planes, each with states of the same class. Horizontal transitions between closed conformations are assumed to be cooperative; however, each closed conformation may lead directly to channel opening in a highly concerted manner. The main difficulty with these models lies in the identification of each state with a particular conformation of the protein. Contrary to this, scheme III may be interpreted as a simple two-tiered version of the MWC model. All the transitions in the closed and the open tiers are cooperative and driven by Ca^{2+} binding steps. Any of the states in the closed tier may lead to opening in a single concerted step, as in the standard MWC model. Planes are originated because one may distinguish the isoforms with two bound Ca^{2+} ions at adjacent subunits, for instance, states C_{10} and O_3 in scheme III, from those where the two Ca^{2+} ions are bound to diagonal subunits of the tetramer, i.e., states C_9 and O_4. Fig. 9 shows a simplified version of scheme III, stressing the localization of the subunit having two bound Ca^{2+} in the open (O_3, O_4) and closed (C_{10}, C_9) conformations (Ca^{2+}-bound subunits are shaded).

Although the analysis here does not allow us to distinguish between two Ca^{2+} bound states (either in diagonal or adjacent subunits), our key result is that the KNF model seems to be sufficient to explain the kinetic properties of single BK channels.

Scheme III was first proposed in Cox et al. (4) for the analysis of macroscopic BK currents. However, there the

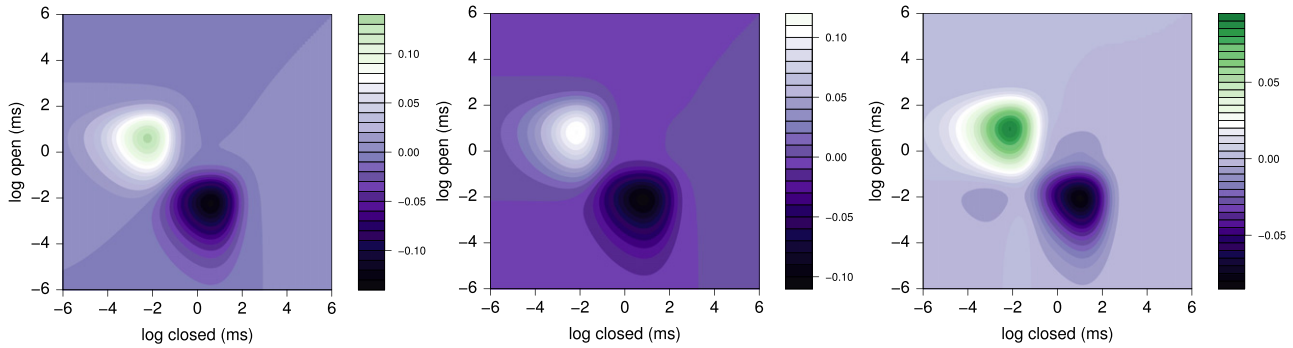

FIGURE 6 Dependency differences at several Ca^{2+} concentrations predicted by the KNF mechanism. From left to right, the Ca^{2+} concentrations are: 1×10^{-7} M, 3×10^{-6} M, and 1×10^{-5} M. Dependency differences are computed by using the predicted joint densities shown in Fig. 5 and their marginals, by following Eq. 6.

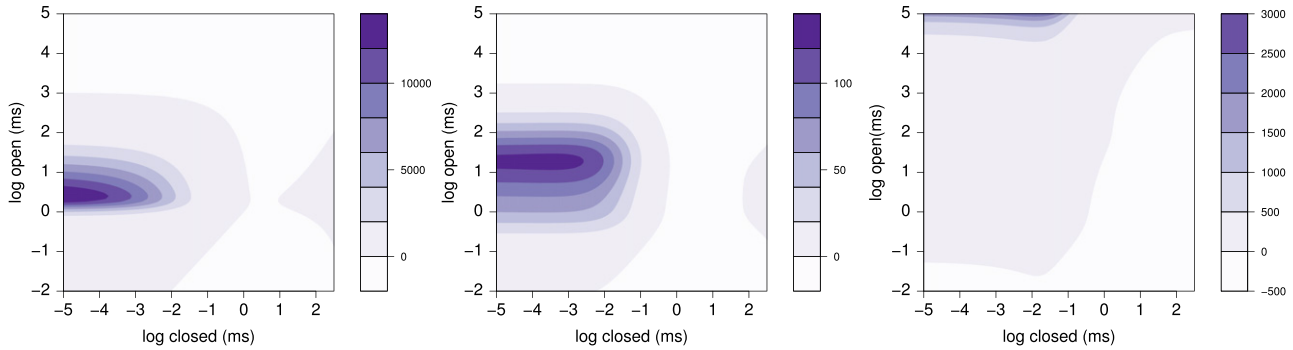

FIGURE 7 Differences at several Ca^{2+} concentrations predicted by the KNF mechanism. From left to right, the Ca^{2+} concentrations are: 1×10^{-7} M, 3×10^{-6} M, and 1×10^{-5} M. Differences are computed by using the predicted joint densities shown in Fig. 5 and their marginals, by following Eq. 7.

transition rates were constrained such as to reduce the number of free parameters down to 10 to be consistent with the standard MWC concerted theory. The resulting model failed to reproduce the conductance-voltage relations at high saturating Ca^{2+} conditions and was superseded by a MWC scheme in which all transition rates are allowed to vary independently from each other. However, (4), but did not consider an unconstrained version of scheme III. On the other hand, the modeling work by the literature (4–6) was directed toward the interrelation between the Ca^{2+} and voltage modulation of BK gating, and did not address the dwell-time properties considered here and in the literature (12–14). It will surely be interesting to see how our estimate for scheme III is able to reproduce some of the properties such as conductance-voltage relations and macroscopic currents.

Recent evidences from heterologous expression of BK channels and site-directed mutations suggest the existence of low and high affinity Ca^{2+} binding sites with distinct properties (26–28). These findings may be the reason explaining the better performance of scheme III at high Ca^{2+}, since this model assumes the existence of six binding sites, instead of just four as done by the other models. Obviously, the different affinities of binding sites were not explicitly taken into consideration by the models here analyzed. This is indeed a new and interesting open problem to be addressed in future modeling work.

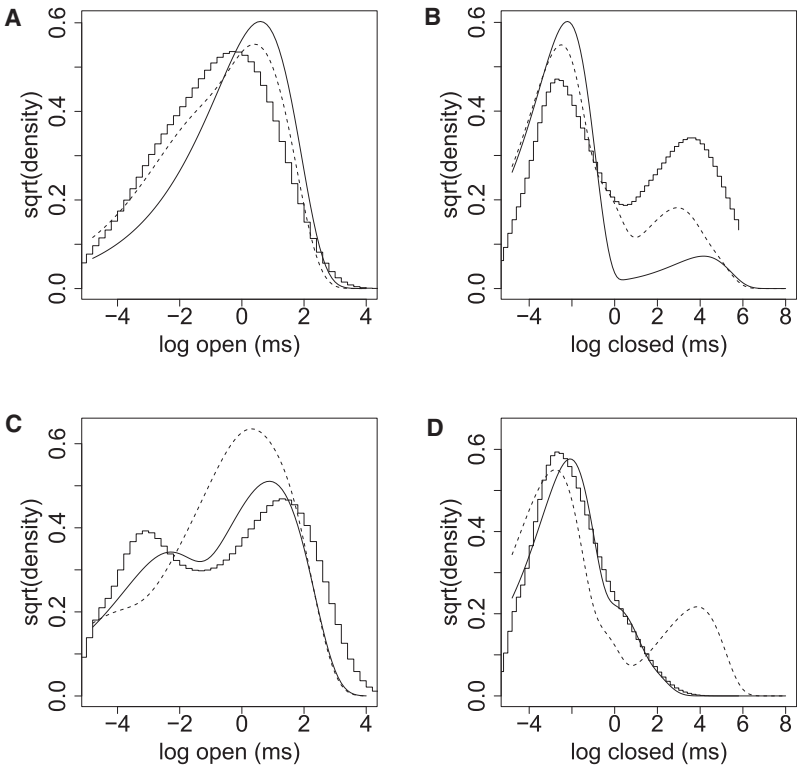

FIGURE 8 Single class dwell-time densities for the two models with highest BIC score, and for a standard filter and threshold analysis at 7.5 KHz. The densities for scheme III are shown as a continuous line, those for scheme IV with a dashed line, and those for the filter and threshold analysis as steps. Panels *A* and *B* present the densities that correspond to the lowest Ca^{2+} condition, and panels *C* and *D* those for the highest Ca^{2+} concentration.

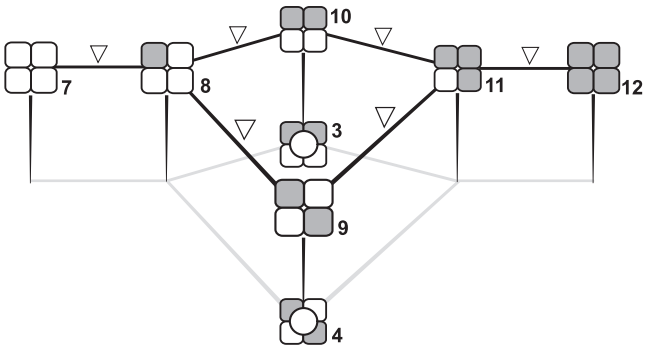

FIGURE 9 A physical interpretation for scheme III.

SUPPORTING MATERIAL

Supporting Material is available at http://www.biophysj.org/biophysj/supplemental/S0006-3495(09)00593-1.

We thank Luiz Bezerra for help while using a SUN Fire x4200 workstation (Pronex/CNPq No. 661036/1998-7) and Jose F. Aguiar for technical assistance with patch-clamp experiments. We also thank the anonymous referees for helpful comments and corrections.

This work was supported by Fundação de Amparo à Pesquisa do Estado de São Paulo grant No. 2005/02063-3 (R.A.R.) and No. 2006/50954-7 (W.A.V.).

REFERENCES

1. McManus, O. B., and K. L. Magleby. 1988. Kinetic states and modes of single large-conductance calcium-activated potassium channels in cultured rat skeletal muscle. *J. Physiol.* 402:79–120.
2. McManus, O. B., and K. L. Magleby. 1989. Kinetic time constants independent of previous single-channel activity suggest Markov gating for a large conductance Ca-activated K channel. *J. Gen. Physiol.* 94:1037–1070.
3. McManus, O. B., and K. L. Magleby. 1991. Accounting for the Ca^{2+}-dependent kinetics of single large-conductance Ca^{2+}-activated K^+ channels in rat skeletal muscle. *J. Physiol.* 443:739–777.
4. Cox, D. H., J. Cui, and R. W. Aldrich. 1997. Allosteric gating of a large conductance Ca-activated K^+ channel. *J. Gen. Physiol.* 110:257–281.
5. Cui, J., D. H. Cox, and R. W. Aldrich. 1997. Intrinsic voltage dependence and Ca^{2+} regulation of mSlo large conductance Ca-activated K^+ channels. *J. Gen. Physiol.* 109:647–673.
6. Cui, J., and R. W. Aldrich. 2000. Allosteric linkage between voltage and Ca^{2+}-dependent activation of BK-type mSlo1 K^+ channels. *Biochemistry.* 39:15612–15619.
7. Horrigan, F. T., J. Cui, and R. W. Aldrich. 1999. Allosteric voltage gating of potassium channels I. mSlo ionic currents in the absence of Ca^{2+}. *J. Gen. Physiol.* 114:277–304.
8. Horrigan, F. T., and R. W. Aldrich. 1999. Allosteric voltage gating of potassium channels II. mSlo channel gating charge movement in the absence of Ca^{2+}. *J. Gen. Physiol.* 114:305–336.
9. Horrigan, F. T., and R. W. Aldrich. 2002. Coupling between voltage sensor activation, Ca^{2+} binding and channel opening in large conductance (BK) potassium channels. *J. Gen. Physiol.* 120:267–305.
10. Monod, J., J. Wyman, and J. P. Changeux. 1965. On the nature of allosteric transitions: a plausible model. *J. Mol. Biol.* 12:88–118.
11. Cox, D. H. 2006. BKCa-channel structure and function. *In* Biological Membrane Ion Channels. S. H. Chung, O. Andersen, and V. Krishnamurty, editors. Springer-Verlag, New York.
12. Rothberg, B. S., and K. L. Magleby. 1998. Kinetic structure of large-conductance Ca^{2+}-activated K^+ channels suggests that the gating includes transitions through intermediate or secondary states. A mechanism for flickers. *J. Gen. Physiol.* 111:751–780.
13. Rothberg, B. S., and K. L. Magleby. 1999. Gating kinetics of single large-conductance Ca^{2+}-activated K^+ channels in high Ca^{2+} suggest a two-tiered allosteric gating mechanism. *J. Gen. Physiol.* 114:93–124.
14. Rothberg, B. S., and K. L. Magleby. 2000. Voltage and Ca^{2+} activation of single large-conductance Ca^{2+}-activated K^+ channels described by a two-tiered allosteric gating mechanism. *J. Gen. Physiol.* 116:75–99.
15. Rosales, R. A. 2004. MCMC for hidden Markov models incorporating aggregation of states and filtering. *Bull. Math. Biol.* 66:1173–1199.
16. Chung, S. H., J. B. Moore, L. Xia, L. S. Premkumar, and P. W. Gage. 1990. Characterization of single channel currents using digital signal processing techniques based on hidden Markov Models. *Philos. Trans. R. Soc. Lond. B Biol. Sci.* 329:265–285.
17. Ventakaramanan, L., and F. J. Sigworth. 2002. Applying hidden Markov models to the analysis of single ion channel activity. *Biophys. J.* 82:1930–1942.
18. de Gunst, M. C. M., H. R. Künsh, and J. G. Schouten. 2001. Statistical analysis of ion channel data using hidden Markov models with correlated state-dependent noise and filtering. *J. Am. Stat. Assoc.* 96:805–815.
19. Golub, G. H., and C. F. Van Loan. 1989. Matrix Computations, 2nd Ed. Johns Hopkins University Press, Baltimore, Maryland.
20. Colquhoun, D., and A. G. Hawkes. 1982. On the stochastic properties of bursts of single ion channel openings and of clusters of bursts. *Phil. Trans. Roy. Soc. Lond. B.* 300:1–59.
21. Colquhoun, D., and A. G. Hawkes. 1995. The principles of the stochastic interpretation of ion-channel mechanisms. *In* Single Channel Recording. B. Sackmann and E. Neher, editors. Plenum Press, New York.
22. Colquhoun, D., and F. J. Sigworth. 1995. Fitting and statistical analysis of single-channel records. *In* Single Channel Recordings. B. Sackmann and E. Neher, editors. Plenum Press, New York.
23. Magleby, K. L., and L. Song. 1992. Dependency plots suggest the kinetic structure of ion channels. *Proc. R. Soc. Lond. B. Biol. Sci.* 249:133–142.
24. Rosales, R. A., W. J. Fitzgerald, and S. B. Hladky. 2002. Kernel estimates for one- and two-dimensional ion channel dwell time densities. *Biophys. J.* 82:29–35.
25. Carnio, E. C., and W. A. Varanda. 1995. Calcium-activated potassium channels are involved in the response of mouse Leydig cells to human chorionic gonadotropin. *Braz. J. Med. Biol. Res.* 28:813–824.
26. Bao, L., A. M. Rapin, E. C. Holmstrand, and D. H. Cox. 2002. Elimination of the BK(Ca) channel's high-affinity Ca^{2+} sensitivity. *J. Gen. Physiol.* 120:173–189.
27. Xia, X. M., X. Zeng, and C. J. Lingle. 2002. Multiple regulatory sites in large-conductance calcium-activated potassium channels. *Nature.* 418:880–884.
28. Sweet, T., and D. H. Cox. 2008. Measurements of the BK_{Ca} channel's high-affinity Ca^{2+} binding constants: effects of membrane voltage. *J. Gen. Physiol.* 132:491–505.